

AN ABSTRACT OF THE THESIS OF

Yuting Xi for the degree of Master of Science in Electrical and Computer Engineering presented on April 27, 2017.

Title: Optofluidic Sensing from Inkjet-Printed Droplets on Diatom Biosilica

Abstract approved: \_\_\_\_\_

Alan X. Wang

We explored an optofluidic sensing mechanism from inkjet-printed droplets on diatom biosilica using surface-enhanced Raman scattering (SERS). Our study revealed a new biosensing strategy that combines the microscopic fluidic flow induced by the droplet evaporation and the photonic crystal effects of diatom frustules, which can provide an ultra-sensitive, cost-effective biosensing technology with reduced analyte consumption enormous improvement of detection limit by  $10^6\times$ . Different than the traditional analyte dispensing method using pipette, inkjet printing technology not only minimizes the analyte consumption and prevents coffee rings, but also facilitates significant molecule accumulation on the hydrophilic surface of the diatom frustule during the evaporation process of sub-nanoliter volume droplets, called the evaporation-induced spontaneous flow effect. We achieved single-molecule-level detection of Rhodamine 6G (R6G) and label-free Trinitrotoluene (TNT) sensing at  $10^{-12}$  M in aqueous solution.

©Copyright by Yuting Xi  
April 27, 2017  
All Rights Reserved

Optofluidic Sensing from Inkjet-Printed Droplets on Diatom Biosilica

by  
Yuting Xi

A THESIS

submitted to

Oregon State University

in partial fulfillment of  
the requirements for the  
degree of

Master of Science

Presented April 27, 2017  
Commencement June 2017

Master of Science thesis of Yuting Xi presented on April 27, 2017

APPROVED:

---

Major Professor, representing Electrical and Computer Engineering

---

Director of the School of Electrical Engineering and Computer Science

---

Dean of the Graduate School

I understand that my thesis will become part of the permanent collection of Oregon State University libraries. My signature below authorizes release of my thesis to any reader upon request.

---

Yuting Xi, Author

## ACKNOWLEDGMENTS

I would like to thank my advisor Dr. Alan Wang for his full support throughout my two and a half years as an MS candidate, providing me with professional guidance, understanding, and encouragement. In addition, I would also like to thank Dr. Larry Cheng, Dr. Matthew Johnston, and Dr. Malhotra for taking the time to serve as my committee members, and for their great questions. My sincerest gratitude goes out to Dr. Larry Cheng for his help in the lab, and Postdoc Xianming Kong for aiding in my research. To all members of Dr. Wang's Group, I thank you for your assistance and professional collaboration.

Thank you to my colleagues at OSU: Ye Liu, Zheng Zhou, Paul LeDuff, and Akash Kannegull. Thank you all for helping me in Lab, it's been wonderful to work with you, and have fun all these years.

Finally, I would like to thank my parents for all their support over the past two years.

# TABLE OF CONTENTS

	<u>Page</u>
Chapter 1: Introduction.....	1
1.1 Introduction to Raman Spectroscopy.....	1
1.1.1 Raman Scattering.....	1
1.1.2 Surface Enhanced Raman Spectroscopy (SERS) Technology.....	2
1.2 Introduction to Optofluidic Sensing.....	2
1.2.1 History of Microfluidic Sensing.....	2
1.2.2 Optofluidic Sensing.....	3
1.3 Photonic Crystal Bio-Silica.....	5
1.4 Inkjet Printing Technology.....	8
Chapter 2: Basic Inkjet Printing Calibration.....	9
2.1 Basic Characteristics of Inkjet Printing Technology.....	9
2.1.1 Inkjet Device.....	9
2.1.2 Dynamic Process of Inkjet Printing.....	11
2.1.3 Droplet Size and Evaporating Time.....	12
2.1.4 Evaporating Process Disparity Between Porous Structures and Hydrophobic Surfaces.....	14
Chapter 3: SERS Sensing from Inkjet-Printed Droplets.....	15
3.1 Materials and Methods.....	15
3.1.1 Materials and Reagents.....	15
3.1.2 Preparation of Diatom Bio-Silica with Photonic Crystal Features.....	15
3.1.3 In-situ Grown Method.....	16
3.1.4 Preparation of Self-Assembled Diatom Substrates with Ag NPs.....	19
3.1.5 Instruments and Measurements.....	20
3.2 Result and Discussion.....	20
3.2.1 Characterization and Integration of Ag NPs on Diatom Bio-Silica.....	20
3.2.2 Optofluidic Sensing from Inkjet Printed Droplets.....	23
3.2.3 Technic Demonstration by Inkjet Printing on TNT Sensing.....	32
Chapter 4: Conclusion.....	35
Chapter 5: Clarification and Acknowledgement.....	36
Chapter 6: Reference.....	37

## LIST OF FIGURES

<u>Figure</u>	<u>Page</u>
Fig. 1 Illustration of rationally designed nanophotonic sensors: (a) micro-ring resonator, (b) PCF, (c) PCW microcavity, (d) plasmonic photonic crystals; (e) GMR grating, (f) plasmonic nanoantennas, (g) Flow-through and flow-over plasmonic sensors, together with each system's sensing response, (h) Fabry-Pérot sensor with flow-through micro- and nanofluidic channels, (i) metamaterials with Fano-resonance, and (j) metamaterials by electroplated nanowires. ....	4
Fig. 2(a) Schematic of 3-D photonic crystals consisting of periodic array of dielectric materials; (b) PBG of 3-D photonic crystals with big refractive index contrast such as semiconductors/air; (c) silicon photonic crystal waveguide fabricated by e- beam lithography and RIE, and (d) GMR-enhanced SERS sensors. ....	6
Fig. 3 SEM images of various diatom species with different frustules <sup>52</sup> .....	7
Table 1: The recommended firing conditions of four commonly used thermal tips. ....	10
Fig. 4 Setup of the inkjet printing system. ....	11
Fig. 5 Actual shape of a single droplet dispensed on a diatom substrate at the first moment. ....	12
Fig. 6 Evaporating process of a single droplet dispensed on diatom frustule.....	13
Fig. 7 Illustration of the microscopic fluid flow process through evaporating of the dispensed sub-nanoliter droplets from the photonic crystal biosilica <sup>72</sup> . ....	14
Fig. 8 An SEM image of deposited Ag seeds on the diatom frustule by in-situ growth method (a) and assembled Ag NPs on diatom frustule by self-assembly method (b) <sup>71</sup> . ....	17
Fig. 9 The SERS spectra of R6G on in-situ-grown SERS substrates and self-assembly substrates at different concentrations of AgNO <sub>3</sub> . ....	18
Fig. 10 SEM images of a single Pinnularia diatom frustule (a) and a zoomed view of sub-micron porous structures (b) <sup>72</sup> .....	21
Fig. 11 SEM images of self-assembled diatom-Ag NPs substrate (a), self-assembled diatom-Ag NPs substrate prepared by 3x concentrated Ag Colloid (b), and in-situ growth diatom-Ag NPs substrate(c) <sup>72</sup> ...	22
Fig. 12 Microscopy image of bare diatom frustules (a) and in-situ growth diatom-Ag NPs (b). ....	22
Fig. 13 Fluorescence microscopy images of diatom substrate excited by white and grey light(a) and yellow light(b).....	24
Fig. 14 Fluorescence microscopy optical image of the printed diatom substrate (a), Fluorescence spectra from the diatom substrate dispensed via pipette and inkjet printer (b), and fluorescence spectra from diatom and glass substrate by the inkjet printer and pipette (c). ....	25
Fig. 15 Comparison of the Raman spectra conducted on diatom-Ag NPs and on glass-Ag NPs SERS substrate. ....	27

## LIST OF FIGURES

<u>Figure</u>	<u>Page</u>
Fig. 16 Comparison of different droplets with fixed concentration of probe molecule solution.....	28
Fig. 17 Comparison of inkjet printing technology and traditional pipette delivery.....	29
Fig. 18 Comparison of different numbers of droplets with the same amount of probe molecules on diatom-Ag NPs substrates (a), on glass-Ag NPs substrates (b) and SERS intensity collected from the most prominent peak of $1360\text{cm}^{-1}$ versus different numbers of droplets (c).....	30
Fig. 19 Ultra-sensitive single molecule detection with diatom substrate by an inkjet printer dispensing 2000 droplets: SERS spectra of $10^{-16}$ M R6G aqueous solution.....	32
Fig. 20 Ultra-sensitive single molecule detection with diatom substrate by an inkjet printer dispensing 2000 droplets SERS spectra of TNT with concentration at $10^{-11}\text{M}$ , $10^{-12}\text{M}$ , and $10^{-13}\text{M}$ . ....	33
Fig. 21 SERS mapping image collected from $10^{-5}\text{M}$ TNT aqueous solution with 400 droplets dispersed on a single diatom and corresponding diatom image (b).....	34

## Chapter 1: Introduction

### Introduction

#### *1.1 Introduction to Raman Spectroscopy*

##### *1.1.1 Raman Scattering*

Raman Scattering was introduced in 1928 by C.V. Raman, an Indian physicist, earning him the 1930 Nobel Prize for Physics<sup>1</sup>. Raman and his students discovered ‘the Raman Effect’ by changing the wavelength of scattered monochromatic visible light. In chemistry and biology, Raman spectroscopy identifies molecules by observing the vibration and rotation of chemical bonds. Raman scattering is an inelastic scattering process. It includes two possible kinds of scatterings: Stokes scattering and anti-Stokes scattering.

In the Stokes scattering process, the energy of the emitted photon is lower than that of the absorbed photon, meaning the material (the molecule) absorbs more energy. In the anti-Stokes scattering process, the energy of the photon emitted from the material is higher than that of the absorbed photon. However, the Raman effect is very weak: three to five orders of magnitude less than Rayleigh scattering, which means an original Raman signal is difficult to detect. This leads us to Surface Enhanced Raman Spectroscopy.

### *1.1.2 Surface Enhanced Raman Spectroscopy (SERS) Technology*

Surface Enhanced Raman Spectroscopy (SERS) is a Raman Spectroscopy-based technology that can enhance the intensity of the Raman signal by six to fourteen orders of magnitude. SERS was discovered by Martin Fleischmann, Patrick J. Hendra, and A. James McQuillan in 1974. Since then, SERS technology has been widely used as an analytical tool in circumstances where there are ultra-low concentrations of target molecules to help identify the analytes<sup>2,3</sup>. Due to its high accuracy and low-concentration functionality, the technology has continued to attract researchers over the decades. SERS greatly enhances Raman scattering signals by the contributing local electromagnetic field enhancements evoked by localized surface plasmon resonance (LSPR)<sup>4-6</sup>.

When light strikes small metal particles, it causes fluctuations in the electric field within, causing electrons to sway and shake in a state called a plasmon. The biased electrons on the surface of the metal create a strong electric field, and when two particulates get close, an extremely strong electromagnetic field is generated between them; this is called a hot spot<sup>7, 8</sup>. In theory, the LSPR (localized surface plasmon resonance) enhances the local and scattered fields around the particle. The intensity of the Raman scattering is proportional to the fourth order of magnitude of the optical electromagnetic field. Due to the extremely strong electromagnetic field, hot spots create large SERS enhancement factors, which provide the most benefit<sup>9</sup>.

## *1.2 Introduction to Optofluidic Sensing*

### *1.2.1 History of Microfluidic Sensing*

Microfluidics is a rapidly developing field that focuses on the precise control and manipulation of the flow of complex fluids at an ultra-small scale. A relatively new multidisciplinary field, microfluidic technology involves the use of microelectronics, micromechanics, bioengineering, and nanotechnology. Unlike microelectronics, the primary goal is to achieve manipulation of fluid flow function through the construction of a micro-channel system, in addition to reducing the size of the devices used. In most cases, active microfluidic systems are built harmoniously by active micro-components such as micropumps, microvalves, micromixers, microfilters, and microseparators. The use of micro-components allows for ultra-small volumes of fluids to be moved, mixed, and screened, creating numerous applications in the chemical, medical, and life-science fields.

Over the past decade, the field of microfluidics has shown more and more promise for clinical application include protein detection<sup>10</sup>, diagnostics aiding<sup>11</sup>, and biofilm screening<sup>12</sup>. Such technology ranges from devices composed of simple microfluidic channels, to complex devices that can combine fluids, pump liquids, control flow, determine optimal reaction conditions, and much more. The last few years have also seen the emergence of micro-fluidics as a means of enabling small-volume sample manipulation to perform automated functions, such as particle sorting and isolation, cell culturing, and concentration gradient formation<sup>13</sup>. Capillary driven flow<sup>14, 15</sup> and vacuum-driven flow<sup>16</sup> passive fluid actuation have also been reported recently<sup>11</sup>.

### *1.2.2 Optofluidic Sensing*

Recent advances in the fields of photonics and microfluidics have led to the burgeon of optofluidics<sup>13, 17-18</sup>. Photonic and microfluidic architectures are integrated to synergistically enhance function and performance, which is ideal for biological and chemical detection. Nanophotonic sensors are a vital part of this field, greatly surpassing conventional optical sensors in terms of size, sensitivity, specificity, tunability, photostability, and in-vivo applicability<sup>19-25</sup>, by employing innovative nanophotonic structures. These sensors include micro-ring resonators<sup>26-28</sup>, whispering gallery-mode resonators<sup>29</sup>, photonic crystal fibers (PCFs)<sup>30</sup>, photonic crystal waveguides (PCWs)<sup>31</sup>, metamaterials<sup>32</sup>, and surface plasmonic nanostructures<sup>19-24</sup> as shown in Figure 1(a)-(j).

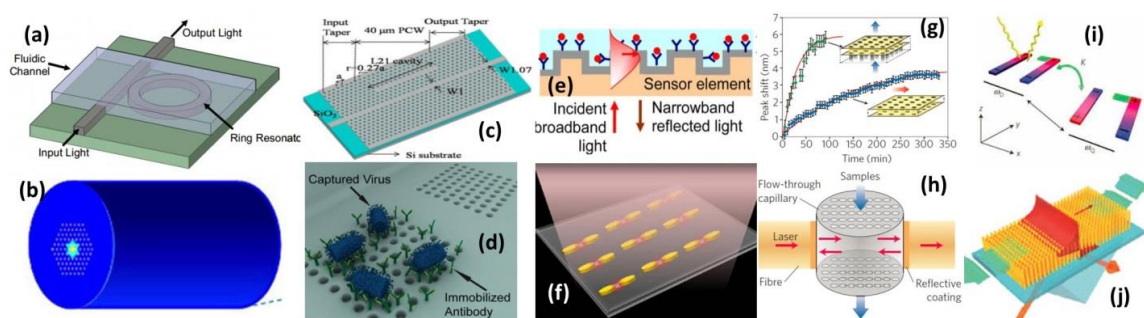


Fig. 1 Illustration of rationally designed nanophotonic sensors: (a) micro-ring resonator, (b) PCF, (c) PCW microcavity, (d) plasmonic photonic crystals; (e) GMR grating, (f) plasmonic nanoantennas, (g) Flow-through and flow-over plasmonic sensors, together with each system's sensing response, (h) Fabry-Pérot sensor with flow-through micro- and nanofluidic channels, (i) metamaterials with Fano-resonance, and (j) metamaterials by electroplated nanowires.

The second most crucial component of optofluidics is the use of microfluidic channels, meaning the detection limitations are based on mass-transport capability instead of detection sensitivity<sup>33</sup>. Because microfluidic channels support laminar flow profiles, the analyte molecules rely on very slow diffusion processes to reach the sensor surface, taking hours to days for sub-picomolar concentration detection. To eliminate this

problem, researchers replaced the ‘flow-over’ technique with a nanofluidic ‘flow-through’ strategy to mitigate the slow mass-transport issues experienced by most optical sensors<sup>34-36</sup>. In such nanofluidic optical sensors, analyte solution flows through semiconductors or plasmonic photonic crystal (PC) sensors (either PC slab or PCF) with sub-micron-scale-arranged air holes as shown in Figure 2(g) and (h). Transporting mass to the sensing surface is almost entirely convective rather than diffusive, providing a stronger signal in significantly less time than the conventional flow-over sensors. Photonic crystals also play an important role, serving as both effective mass-transport channels and ultra-sensitive detectors, especially in designs with strong fields in the air holes.

### *1.3 Photonic Crystal Bio-Silica*

Photonic crystal (PC) is a recent breakthrough that facilitates the manipulation of light<sup>37, 38</sup>. It is comprised of a periodic array of submicron scale, low or high-dielectric-constant materials in a homogeneous dielectric matrix, as shown in Figure 3(a). The periodic, dielectric lattice within the crystal can create frequency bands and frequency gaps in photons, the latter identified as the “photonic band gap (PBG)” in Figure 2(b). Slow-light effects<sup>39</sup> and guided-mode resonances (GMRs)<sup>40</sup> can be observed at optical frequencies near this gap.

Multiple silicon PC devices<sup>41, 42</sup> have been developed by our group. These nanostructures can be beneficial when using highly efficient electro-optical modulators<sup>43</sup>,<sup>44</sup>, highly sensitive infrared absorption sensors<sup>45, 46</sup>, and GMR-enhanced SERS sensors<sup>47</sup>,

as shown in Figure 2(c) and (d). The SERS signals can be strengthened by more than ten times, and the detection limit can be increased by several orders of magnitude through the combination of plasmonic NPs with the rationally designed PC devices.

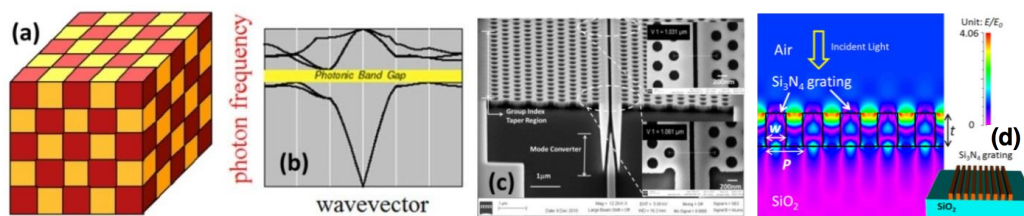


Fig. 2(a) Schematic of 3-D photonic crystals consisting of periodic array of dielectric materials; (b) PBG of 3-D photonic crystals with big refractive index contrast such as semiconductors/air; (c) silicon photonic crystal waveguide fabricated by e- beam lithography and RIE, and (d) GMR-enhanced SERS sensors

Despite their potential benefits, photonic crystal sensors produced by traditional means require costly top-down fabrication techniques and tools such as metal evaporation, photolithography, focused-ion beams (FIBs), and reactive ion etching (RIE). More importantly, even more concerning are the potential environmental repercussions: high energy consumption and low material-usage efficiency of the non-degradable wafers. In addition, many sensors are discarded after only a single use to avoid cross contamination. Fortunately, nature has provided a virtually unlimited source of PC structures in the form of photosynthetic marine microorganisms<sup>48</sup> that use imbedded, inorganic, periodic photonic structures into their cell walls, to efficiently capture sunlight, which is very similar to rationally designed PCs<sup>49-51</sup>.

Unlike artificial PCs made with cost-prohibitive, top-down lithographic and RIE techniques, diatoms create skeletal shells of hydrated amorphous silica, called frustules that possess photonic crystal-like features created by bottom-up approach at

environmental temperatures and pressures. These remarkable microorganisms generate frustules from amorphous silica within an intracellular nano-bioreactor using water-soluble silicic acid. Multiple species of bio-silica-based diatoms and calcium carbonate-based coccolithophores with versatile photonic crystal structures have been used in experiments (Figure 3(a)-(d))<sup>52</sup>. Diatoms have potential for use in solar cells<sup>53</sup>, batteries<sup>54</sup>, drug delivery methods<sup>55</sup>, electro-luminescence<sup>56</sup>, photo-luminescence (PL)<sup>57</sup>, nanofabrication templates<sup>58</sup>, and selective membranes<sup>59</sup>. PL-based diatom biosensors were reported<sup>60</sup> in the past because the PL emission of porous silica is affected when the adsorbed biomolecules donate electrons to non-radiative defect sites on the frustule surface. However, PL sensors are unable to obtain molecular structure information, and cannot compete with the sensitivity of SERS.

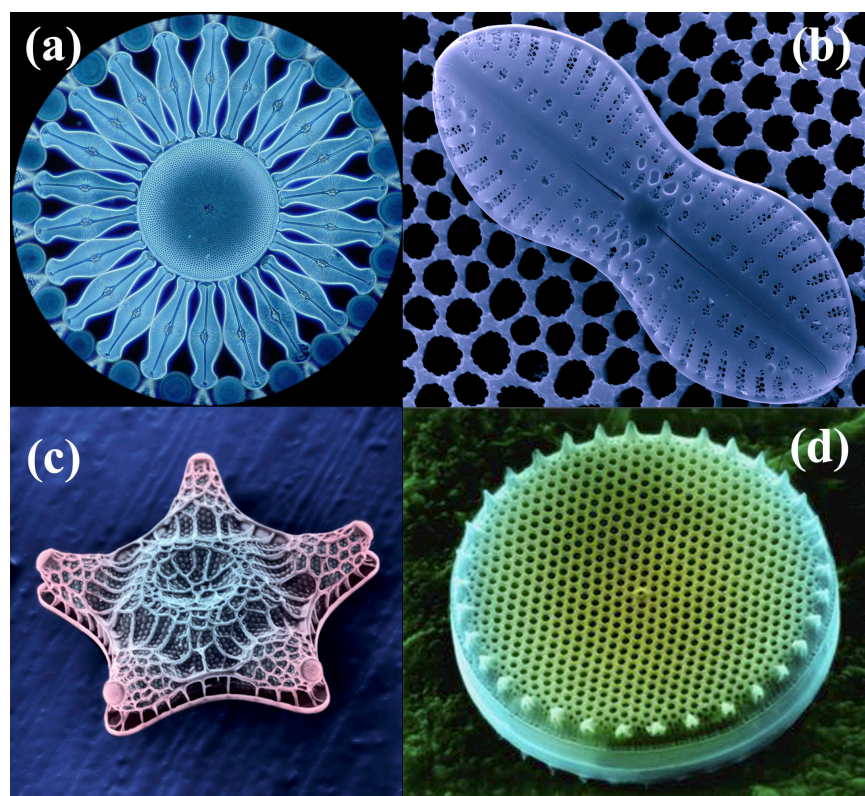


Fig. 3 SEM images of various diatom species with different frustules<sup>52</sup>

### *1.4 Inkjet Printing Technology*

In the past, researchers usually dispensed large droplets of analyte solution directly to the sensor surface. In recent decades, microfluidic devices have been widely used in biosensing. Unlike traditional analyte delivering methods, microfluidic devices allow the delivery of assays at the pico- to nano-liter scale<sup>61-63</sup>, which could help to minimize the usage of analyte. However, microfluidic chips are usually complicated and expensive, as well as too complex to modify the assay-specific surface as required. Inkjet printing technology is a cost-effective technology without the requirement of complex chips; it reduces analyte consumption, and provides much greater usability. Because of its many advantages, researchers have been determined to redesign the inkjet printers for laboratory use to deliver various kinds of biofluid samples.

Previously, inkjet printing technology has been used for the fabrication of plasmonic paper devices<sup>64-66</sup>, conductive circuits<sup>67</sup>, and printing nanoparticle inks to fabricate SERS active patterns<sup>68</sup>. Also, due to its advantage in cost-efficiency, inexpensive materials, waste elimination, and ability to produce ultra-small droplets of fluid, researchers use the inkjet printing technology to fabricate large-scale patterns and devices<sup>69</sup>. The basic idea behind the inkjet printing approach is the use of an inkjet head, fed with small volumes fluid, to deliver multiple miniature droplets to either pinpoint targets or draw complex patterns.

## Chapter 2: Basic Inkjet Printing Calibration

### *2.1 Basic Characteristics of Inkjet Printing Technology*

#### *2.1.1 Inkjet Device*

Currently, there are two main types of drop-by-demand laboratory inkjet printers in use: the piezoelectric inkjet printer and the thermal inkjet printer. The thermal inkjet was used in our experiments. In our design, thermal energy was generated by the inkjet printer, and then a single layer of fluid was heated by the thermal energy. At this point, a small bubble is generated that pumps the same volume of fluid through a nozzle. Drop-by-demand means that all the jetting processes were precisely controlled by programs. All our printing experiments were conducted using a Pico-Fluidic Research stationary thermal inkjet printer from Hewlett-Packard (HP Inc., Corvallis, OR, USA). This research inkjet printer kit is an ultra-low consumption, personal-use tool with a wide range of droplet sizes (down to 1pl, and up to 280pl). It can dispense picoliter-level droplets of solutions by using disposable, multi-sized thermal inkjet tips.

The kit contains a portable inkjet controller body and a large selection of thermal inkjet tips. Different inkjet tips eject different droplet sizes (1pl - 280pl). Also, the firing pulse and firing voltage was adjusted specifically for each tip. In addition, each inkjet tip has a different number of possible nozzles. When it is indicated that an inkjet tip ejected a droplet of 1pl, it was a 1pl droplet ejected from a single nozzle, but there were several

working nozzles to choose from, and all selected nozzles work simultaneously. The #34 thermal tip was used most frequently in our experiments. This kind of tip features twelve nozzles and 100pl of volume for each ejection from a single nozzle. The firing pulse for this type of thermal inkjet tip is 1usec, and the firing voltage is 25 volts. If the voltage is too low, there will not be enough energy to eject the fluid droplets, but too high of voltage will over-heat and damage the resistors in the thermal tip. Table 1 shows the recommended firing conditions of four thermal tips commonly-used in our experiments.

Name	Firing Pulses (usec)	Firing Voltage (V)
Tip #34	1	25
Tip #41	1.5	25
Tip #42	1.6	20
Tip #43	1	20

Table 1: The recommended firing conditions of four commonly used thermal tips.

The controller was operated by an Excel-based software from HP called ‘Tips Beta Program.’ This software can serve multiple purposes, such as size-adjustment, single-droplet-ejection, and multiple-droplet-ejection with adjustable intervals of time. It can also be used to change the desired nozzle type. Figure 4 shows the setup of the inkjet printing system.

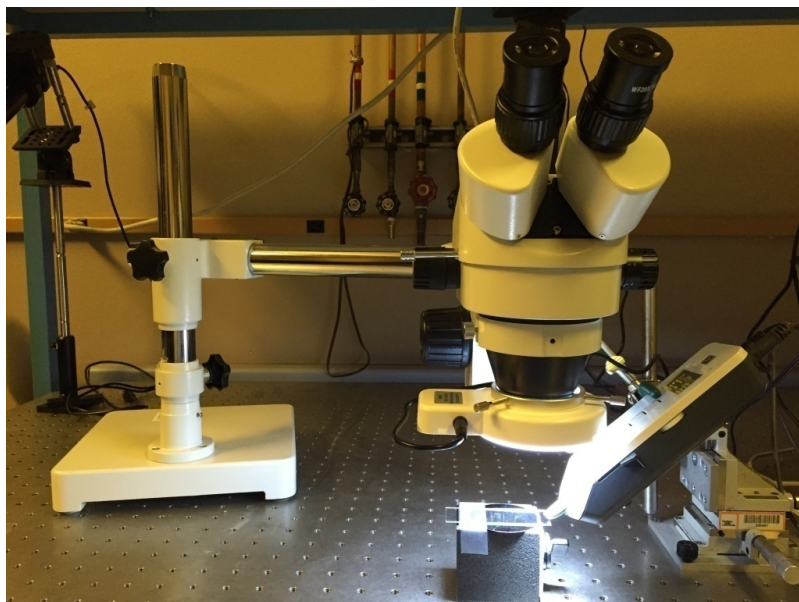


Fig. 4 Setup of the inkjet printing system.

### *2.1.2 Dynamic Process of Inkjet Printing*

A single droplet dispensed from a single nozzle of the #34 thermal tip (the most frequently used tip) will generally cover a circle approximately  $25\mu\text{m}$  in diameter; the actual shape and covered area changes slightly with the dispensing angle unique to each experiment. In our experiment, we fixed the dispensing angle at 45 degrees. Under these conditions, the shape of the landed droplet was sufficient to cover a whole diatom, and

the view through the Microscope was clear. Because of the extremely low mass of a single droplet, the droplets will land across a large area after being dispensed from the inkjet head. In order to solve this problem, I placed the inkjet head 2 mm away from the substrate. Figure 4 displays the actual shape of a single droplet dispensed on a diatom substrate at the first moment. This substrate was prepared by Paul from Dr. Rorrer's group. The average length of a single diatom was around 10  $\mu\text{m}$ , we observed that the approximate diameter of the target droplet was around 30  $\mu\text{m}$ .

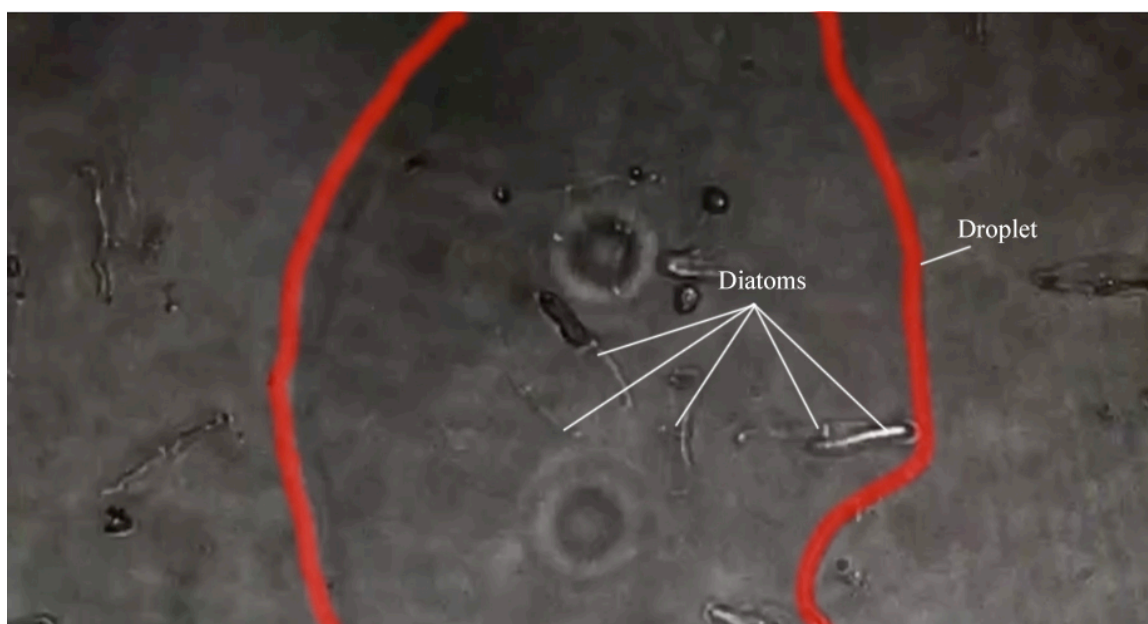


Fig. 5 Actual shape of a single droplet dispensed on a diatom substrate at the first moment.

### *2.1.3 Droplet Size and Evaporating Time*

It featured a 100-picoliter (pl) volume per dispersal from a single selected nozzle, and covered an area of roughly 25  $\mu\text{m}$  in diameter when the inkjet head was perpendicular to the substrate. However, in most cases, we preset the inkjet head at an

angle around 45 degrees. By using this inkjet printing technology, we printed multiple 100-picoliter droplets with accurate targeting onto a prefixed target area, making it possible for label-free detection of target molecules, and greatly reducing analyte consumption.

Normally, the evaporating time of a single 100-picoliter droplet dispensed on diatom frustules will last around 1.1s. During my experiments using multiple droplets, I preset the interval time between two consecutive firing processes, to 1.3s to allow for sufficient evaporation. Figure 6 shows the evaporating process. These discrete time pictures were taken continuously by an Olympus IX73 microscope.

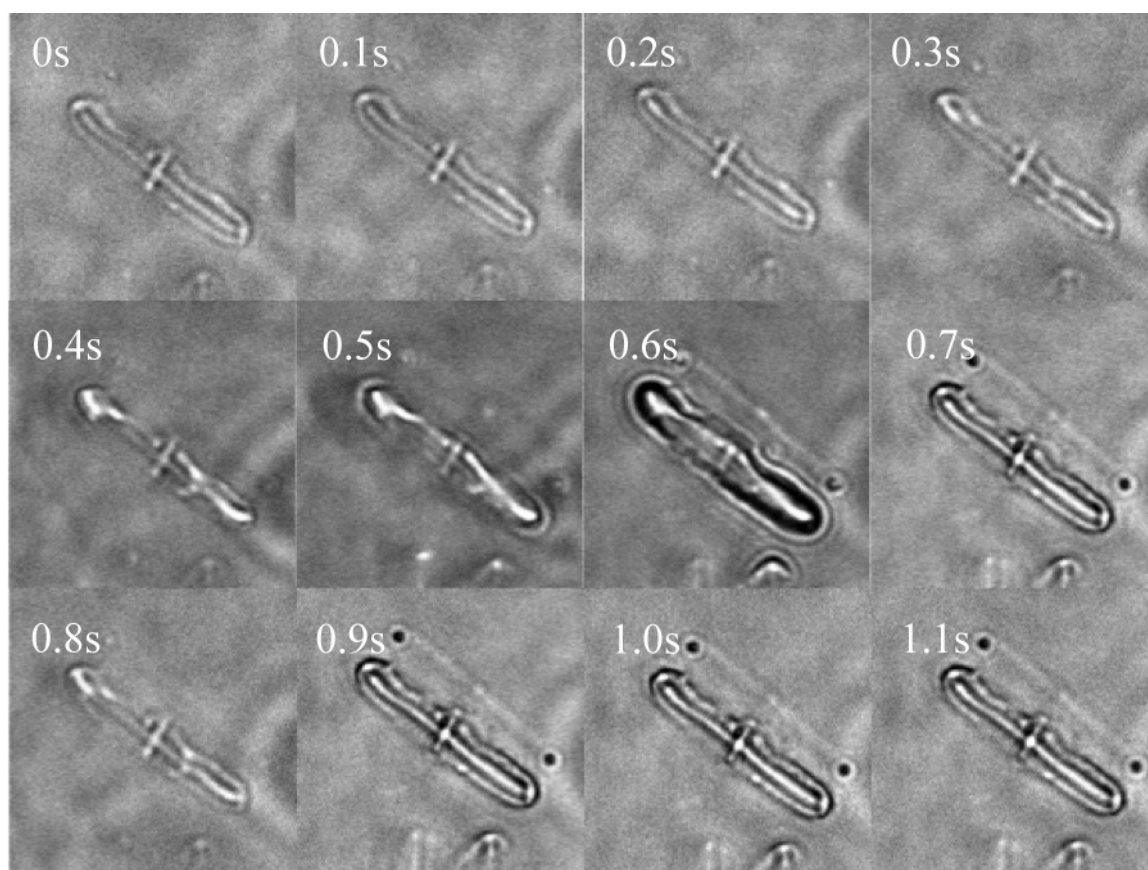


Fig. 6 Evaporating process of a single droplet dispensed on diatom frustule.

### 2.1.4 Evaporating Process Disparity Between Porous Structures and Hydrophobic Surfaces

There is significant difference in evaporating time between a diatom substrate and a glass substrate. Figure 7 from Prof. Tan's work<sup>72</sup> shows the microscopic fluid flow process through evaporating of the dispensed sub-nanoliter droplets from the photonic crystal biosilica. Compared to a plain glass substrate, the diatom-based substrate is more hydrophilic because the features of its porous structure and the abundant hydroxyl groups of diatom frustules. Due to the hydrophilic/hydrophobic feature of the diatom on the glass substrate, the solution liquid will move towards the pores of the diatom frustule during the evaporating process. One such implementation is the accumulation of enormous molecules to the surface of bio-silica, resulting in an increase in SERS sensitivity of  $10^6$  to  $10^7$  times.

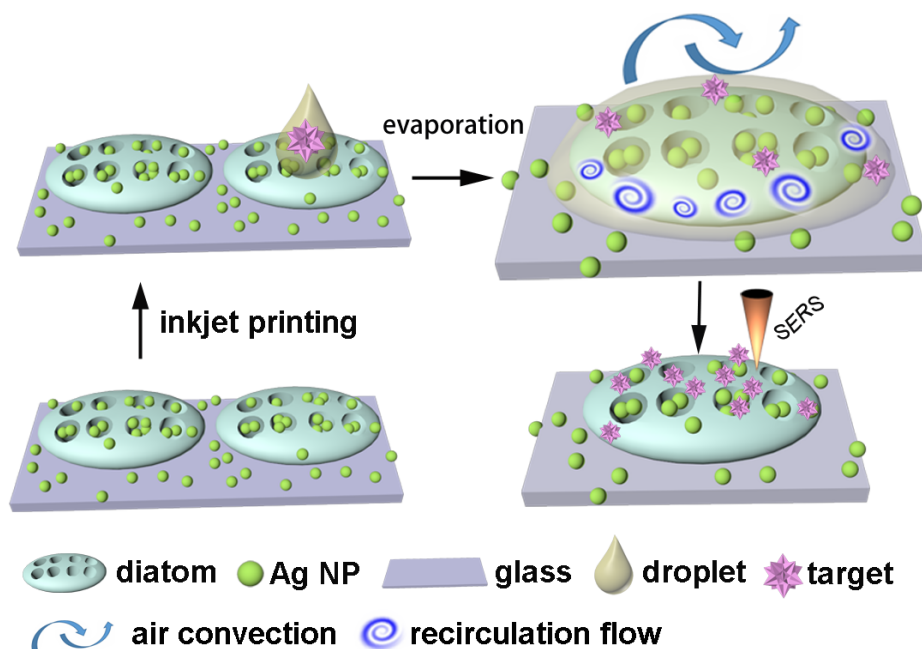


Fig. 7 Illustration of the microscopic fluid flow process through evaporating of the dispensed sub-nanoliter droplets from the photonic crystal biosilica<sup>72</sup>.

## Chapter 3: SERS Sensing from Inkjet-Printed Droplets

### *3.1 Materials and Methods*

#### *3.1.1 Materials and Reagents*

Tin(II) chloride ( $\text{SnCl}_2$ ), Ethylene-diaminetetraacetic acid (EDTA), ascorbic acid, 5,5'-dithiobis (2-nitrobenzoic acid) (DTNB), and poly-diallyldimethylammonium chloride (PDDA) were purchased from Sigma-Aldrich. Silver nitrate ( $\text{AgNO}_3$ ) was obtained from Alfa Aesar. Trisodium citrate ( $\text{Na}_3\text{C}_6\text{H}_5\text{O}_7$ ), sodium hydroxide (NaOH), hydrochloric acid (HCl), ethanol, and acetone were purchased from Macron Chemicals. Rhodamine 6G (R6G) was purchased from TCI. All the deionized (DI) water (18.1 M $\Omega$  cm) used throughout the experiments was purified and deionized by a Milipore Synergy UV Unit.

#### *3.1.2 Preparation of Diatom Bio-Silica with Photonic Crystal Features*

The photonic crystal-laden diatoms (*Pinnularia* sp.) were bought from UTEX Culture Collection. The diatoms were grown on glass substrates, and all the organic materials were removed by hydrogen chloride and hydrogen peroxide. After removing

the organic materials, the diatoms were weighed and dissolved back into 0.1mg/ml ethanol. In the meantime, the plain glass substrates were cleaned by immersing the glass slides into an ultrasonic bath with DI water for 10min, and then the DI water was replaced with the diatom ethanol solution to repeat the process for another 10min, fully coating the substrates with diatom. The substrates were then taken out and dried with nitrogen. After drying, the substrates were loaded into the annealing furnace for one hour at 450° C to bind the diatom with the substrates, and then left to cool for two hours.

### *3.1.3 In-situ Grown Method*

#### *3.1.3.1 Advantages of the in-situ grown method*

The use of in-situ-grown Ag nanoparticles in the diatom substrate technique was first proposed by Tsukruk's group, and was first modified by Xianming Kong in our group. This technique makes it possible to grow Ag NPs directly inside the nano-sized pores of diatoms, which provides a much higher particle density in diatom substrates compared to the self-assembly method<sup>71</sup>. Furthermore, a higher density of nanoparticles provides a sharp increase in the number of hot spots, possibly resulting in a better SERS signal. Figure 8(a) shows an SEM image of the Ag seeds deposited on a diatom frustule through the in-situ growth method, and Figure 8(b) shows the same species of diatom with Ag NPs grown by the self-assembly method. The nanoparticles are successfully settled inside the nano-pores of the frustule in Figure 8(a), and distributed more uniformly. However, the traditional self-assembly method very rarely places nanoparticles into the nano-pores, and the distribution is relatively random.

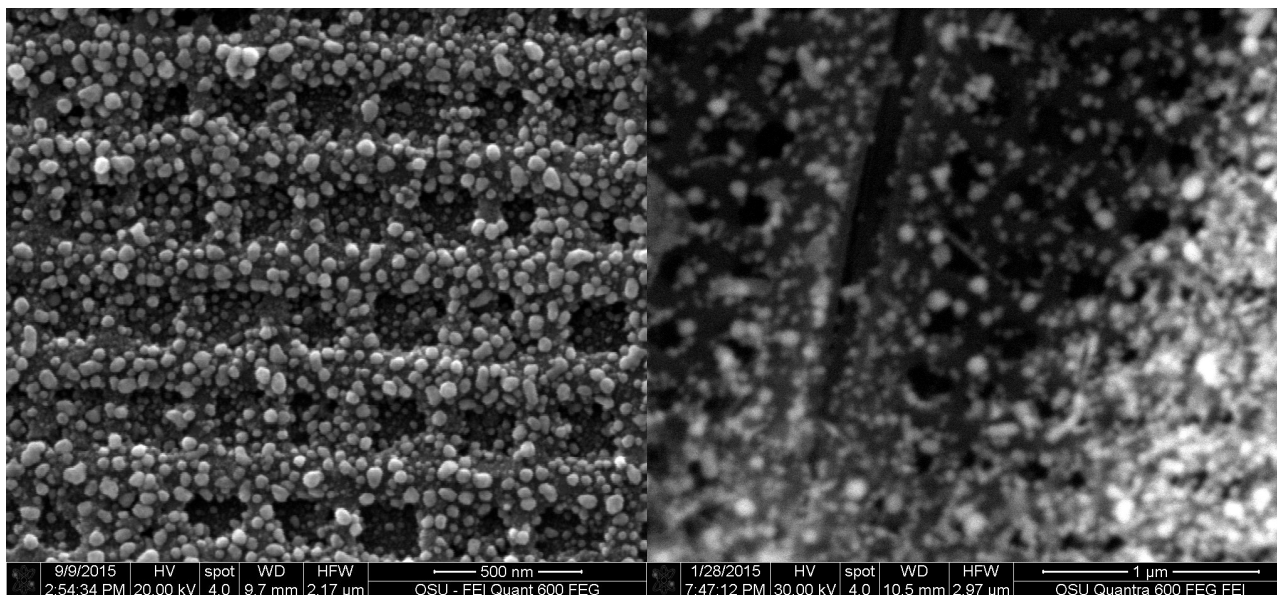


Fig. 8 An SEM image of deposited Ag seeds on the diatom frustule by in-situ growth method (a) and assembled Ag NPs on diatom frustule by self-assembly method (b)<sup>71</sup>.

Figure 8 shows the SERS performance advantage of the in-situ growth SERS substrate in comparison with the traditional self-assembly substrate at different concentrations of  $\text{AgNO}_3$ . In our experiment, R6G was used for probe molecules, and a 532 nm wavelength laser was selected as the excitation light. A height of  $1360 \text{ cm}^{-1}$  was chosen as the characteristic peak. Figure 9(a) and (c) were created from in-situ-grown SERS substrates, and (b) and (d) from the self-assembly substrate. Comparing the two groups, the SERS signals from the in-situ growth had three times the intensity of the self-assembly group.

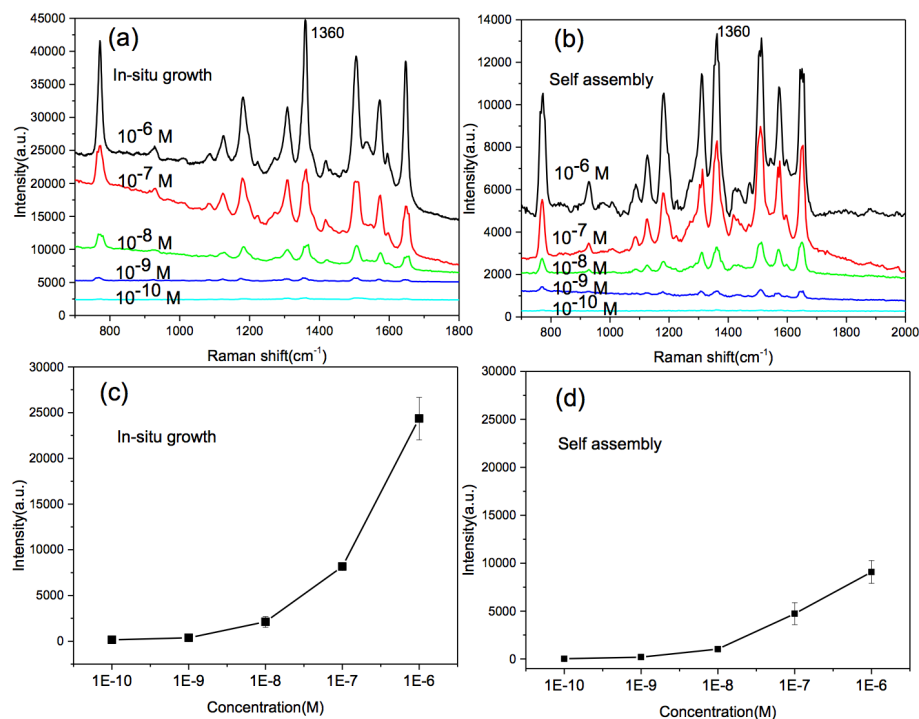


Fig. 9 The SERS spectra of R6G on in-situ-grown SERS substrates and self-assembly substrates at different concentrations of  $\text{AgNO}_3$ .

### 3.1.3.2 Preparation of In-Situ-Grown Substrate

The diatom substrate was briefly immersed into 20mM  $\text{SnCl}_2$  and 20mM HCl aqueous solution, held in place it for 5min to fix the  $\text{Sn}^{2+}$  on the inner wall of the nanopores, and washed with DI water and then acetone. After rinsing, the substrate was dried with nitrogen gas and immersed into 20mM  $\text{AgNO}_3$  aqueous solution for a 5min interval, after which the Ag seeds were deposited onto the diatom frustules, the substrate was rinsed again, and then immersed into a 1mM, 2.5mM, 5mM, and 10mM  $\text{AgNO}_3$  solution with 0.5ml of ascorbic acid. The diatom substrate was kept in the solution for 10min to

ensure the Ag seeds were properly distributed throughout the diatom frustules, and then was removed from the solution, rinsed and dried again.

#### *3.1.4 Preparation of Self-Assembled Diatom Substrates with Ag NPs*

The prepared AgNPs was ellipse-like and 40nm in size; the surface plasmon resonance (SPR) peak of our Ag NPs was at 405nm. The method of synthesizing AgNPs that was followed was first described by Lee and Meisel<sup>35</sup>. Generally, a flask of 250ml, 1mM AgNO<sub>3</sub> aqueous solution was heated in an oil bath, stirred magnetically in the flask, and then boiled. After being boiled, a solution of 5ml 1% sodium citrate was slowly injected into the AgNO<sub>3</sub> solution five times—1ml for each injection—and then boiled for another hour. After the color turned to dark yellow, it was cooled down to room temperature, and then stored in a refrigerator.

In the self-assembly process, the PDDA was diluted one hundred times with DI water. The diatom substrate was immersed into 30ml of diluted PDDA solution for 30min to cationize the substrate. After 30min, it was taken out and thoroughly rinsed with DI water, and then dried with nitrogen. Next, the cationized diatom substrate was immersed into 30 ml AgNPs colloid overnight. Due to the negative charge on the surface of a silver nanoparticle, the nanoparticle was self-assembled on the cationized substrate. The density of silver nanoparticles on the substrate was proportional to the assembly time. After the AgNPs were assembled, they were taken out, thoroughly rinsed, and then dried with nitrogen.

### *3.1.5 Instruments and Measurements*

The inkjet device I used throughout my experiments was the Pico-Fluidic Research stationary thermal inkjet printer from Hewlett-Packard (HP Inc., Corvallis, OR, USA), and was controlled by a kitted software. The SERS measurements included the Raman spectra, and maps were obtained from the Horiba Jobin Yvon Lab Ram HR800 Raman system with a 50x objective lens that was focused manually to obtain better Raman intensity. A 532nm green laser was chosen as the excitation source. Each measurement was taken with 1sec of integration time, and taken twice to produce an average result, thus reducing errors. The diameter of the confocal pinhole was set to 200 $\mu\text{m}$ . Due to the characteristic prominent modes of R6G (1360 $\text{cm}^{-1}$ , 1506 $\text{cm}^{-1}$ , and 1650 $\text{cm}^{-1}$ ), the range of Raman spectra (Raman shift) ranged from 800 $\text{cm}^{-1}$  to 1800 $\text{cm}^{-1}$ . The Raman mapping images were obtained with a 20x20-point mapping array through a 100x objective lens. All ink jetting processes were controlled by the software from HP. Fluorescence images were obtained using the Olympus IX73 microscope. The scanning electron microscopy (SEM) images were obtained from FEI Quanta 600 FEG SEM.

## *3.2 Result and Discussion*

### *3.2.1 Characterization and Integration of Ag NPs on Diatom Bio-Silica*

As shown in Figure 10(a-b), the characterization and integration of Ag NPs on diatom bio-silica images were obtained through scanning electron microscopy (SEM). The morphology and zoomed microscopic structures of the diatom are also shown in figure 10(a-b). Along the horizontal axis, the dimension is around 25 $\mu\text{m}$ ; along the

vertical axis, it is roughly 4-5 $\mu\text{m}$ . The frustules of a diatom bio-silica (pinnularia) are porous structures, patterned with groups of sub-pores. As shown in Figure 10(b), each sub-pore consists of a small pore in the center (50nm) and four larger pores around the center pore (80nm). The diameter of a sub-pore is roughly 200nm.

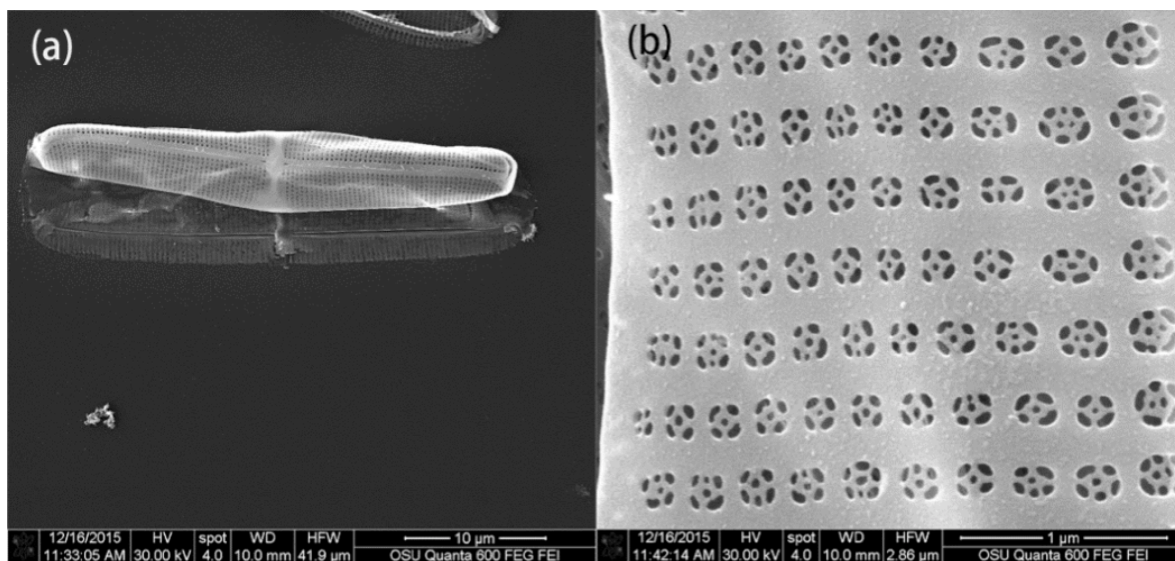


Fig. 10 SEM images of a single Pinnularia diatom frustule (a) and a zoomed view of sub-micron porous structures (b)<sup>72</sup>

The assembly method we used throughout our experiment was the in-situ growth method<sup>72</sup>. Compared to the traditional self-assembly method, the in-situ growth method allows for a much higher density of silver nanoparticles. SEM images of the integration of Ag NPs on diatom frustules show in Figure 11—Figure 11(a) and (b) are images of diatom substrates with Ag NPs assembled by traditional self-assembly method (the substrate shown in Figure 11(b) was assembled by 3x concentrated silver colloids), and Figure 11(c) shows an image of the diatom-Ag Nps—that an Ag NPs substrate was successfully created using the novel in-situ, in-pore growth method.

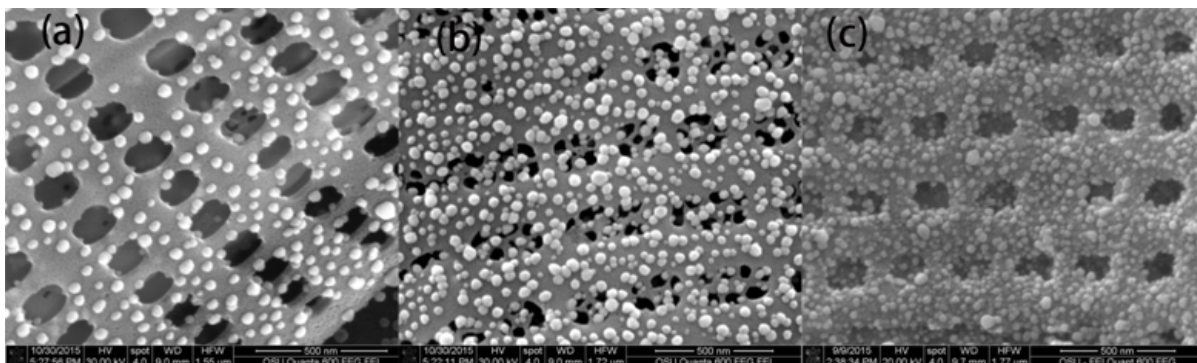


Fig. 11 SEM images of self-assembled diatom-Ag NPs substrate (a), self-assembled diatom-Ag NPs substrate prepared by 3x concentrated Ag Colloid (b), and in-situ growth diatom-Ag NPs substrate(c)<sup>72</sup>.

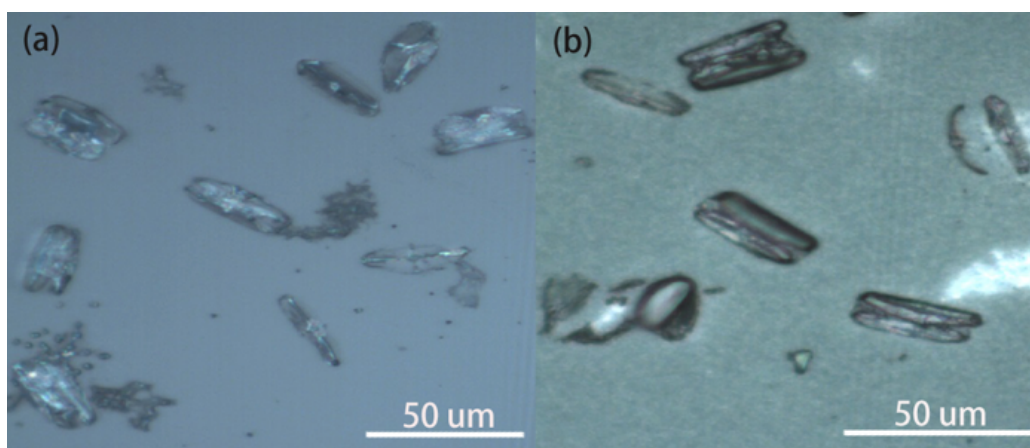


Fig. 12 Microscopy image of bare diatom frustules (a) and in-situ growth diatom-Ag NPs (b).

The higher density silver colloid was prepared by centrifuging. We observed that even the substrate prepared using a silver colloid with three times the density still resulted in a much lower density in the assembled Ag NPs than the in-situ method (Figure 11(c)). It is possible that the repulsion of electrostatic force used in the self-assembly method is responsible for this effect. However, using the in-situ growth method, the Ag NPs were integrated into the diatom frustules. When the diatoms were immersed into the  $\text{AgNO}_3$

solution, the Ag seeds were coating the entire surface and inner walls. Figure 12 is the microscopy image of bare diatom frustules and in-situ growth diatom-Ag NPs. We observed that the Ag NPs are distributed very uniformly on the frustules.

### 3.2.2 *Optofluidic Sensing from Inkjet Printed Droplets*

#### 3.2.2.1 *Fluorescence Measurement*

Due to the large difference in the wettability between a glass surface and a diatom frustule, during the evaporating process, liquid will flow toward the diatom frustule as it evaporates. To demonstrate the analyte enrichment effect of diatom, we used R6G as probe molecules. R6G is used for color dye and probe molecules because of its fluorescence color. An amount of  $2\mu\text{l}$   $10^{-4}\text{M}$  R6G aqueous solution was dropped on the diatom substrate, and then excited by color. The fluorescence microscopy images were collected as shown in Figure 13.

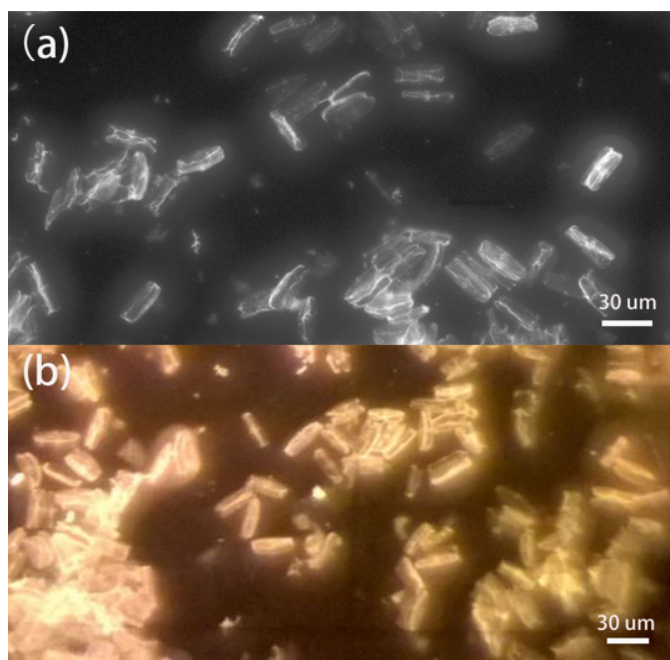
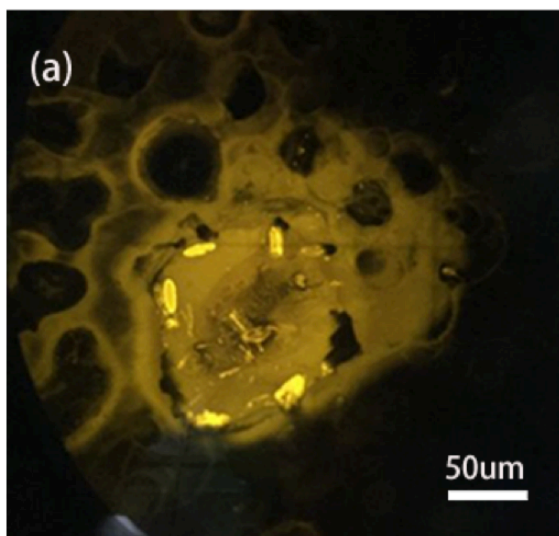


Fig. 13 Fluorescence microscopy images of diatom substrate excited by white and grey light(a) and yellow light(b).

We also used fluorescence measurement to verify the advantages of the inkjet printing strategy. We first dispensed 200 droplets of R6G aqueous solution concentrated at  $10^{-7}$ M onto the diatom substrate by inkjet printer. After dispersal, we took the measurement of the fluorescence excited by the green laser. Figure 14(a) is the fluorescence microscopy optical image of the printed diatom substrate, which shows a stark contrast between diatoms and their surroundings, meaning there are much more probe molecules captured by diatoms. It has also demonstrated that the evaporation-induced liquid flow effect can transport probe molecules onto the surface of diatom frustules.



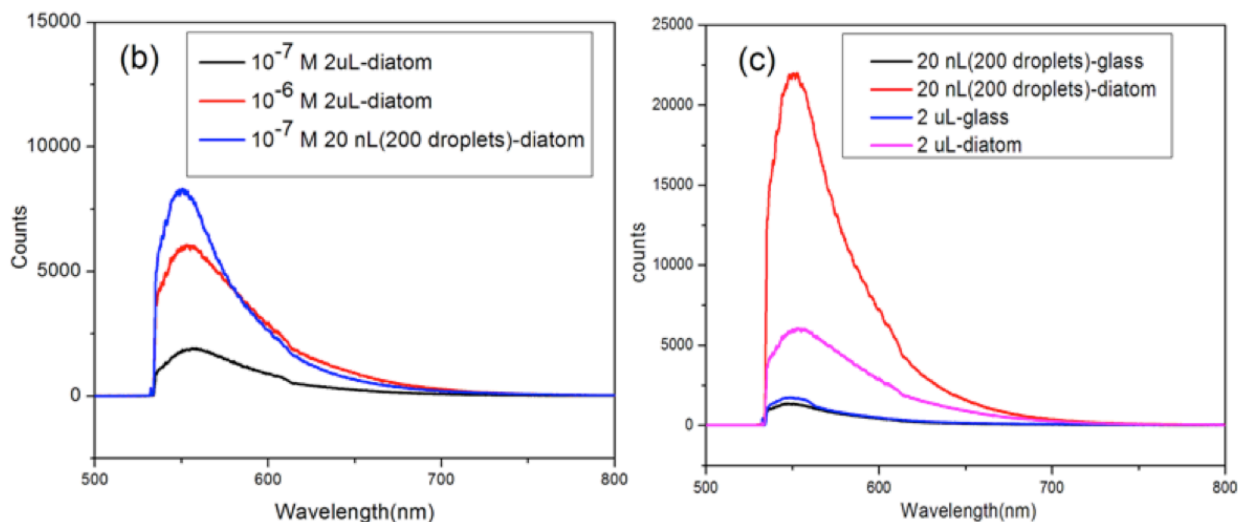


Fig. 14 Fluorescence microscopy optical image of the printed diatom substrate (a), Fluorescence spectra from the diatom substrate dispensed via pipette and inkjet printer (b), and fluorescence spectra from diatom and glass substrate by the inkjet printer and pipette (c)<sup>71</sup>.

The evaporation-induced liquid flow effect was also demonstrated by fluorescence spectra from Figure 14(b). We dispensed 200 droplets  $10^{-7}$ M of R6G aqueous solution on diatom substrates by inkjet printer, and dropped 2 $\mu$ L  $10^{-6}$ M and  $10^{-7}$ m of R6G aqueous solution by pipette. All three measurements were taken on diatom substrate. The fluorescence spectra from the inkjet printing strategy shows significantly greater intensity than the  $10^{-7}$ M trial via pipette, which has same amount of probe molecules as the amount dispensed by inkjet printer. The spectra from the inkjet printer also shows a significantly greater intensity than the  $10^{-6}$ M trial, which has 10 times more probe molecules than those dispensed from the inkjet printer. It proves that the ultra-small droplets dispensed from the inkjet printer can further enhance the accumulation of probe molecules.

We took a third measurement to demonstrate the molecule accumulation ability of the inkjet printing technique by taking a fluorescence spectral of  $10^{-6}$ M of R6G aqueous solution on diatom and bare glass from 200 droplets dispensed by both inkjet printer and pipette. The total number of probe molecules was the same among those four groups. As the results show in Figure 14(c), the fluorescence intensity collected from the two inkjet-printed groups shows a difference of roughly 17 times. The diatom substrate shows a substantially greater intensity than the glass substrate. However, the result from the other two groups only shows a difference of roughly three times. This proves that the inkjet printing technique can effectively enhance the SERS intensity through the evaporation-induced liquid flow effect of ultra-small droplets

### *3.2.2.2 Demonstration of the Evaporation-Induced Liquid Flow via SERS Measurement*

We began by researching the sensitivity of SERS sensing of the hybrid plasmonic-bio-silica (diatom) based platform via in-pore synthesized Ag NPs. The probe molecule we used was R6G, which features characteristic peaks at  $1307\text{cm}^{-1}$ ,  $1360\text{cm}^{-1}$ ,  $1506\text{cm}^{-1}$ , and  $1650\text{cm}^{-1}$ . An amount of  $1\mu\text{l}$   $10^{-6}$ M R6G aqueous solution was dropped onto the SERS substrate via pipette, and then dried it by nitrogen. After drying, SERS measurements of diatom basilica and bare glass-AP NPs were taken. Both were conducted with a similar density of Ag NPs attachment. Figure 15 shows the comparison of the Raman spectra conducted on diatom-Ag NPs and on glass-Ag NPs SERS substrate. As seen in Figure 15, the SERS signals conducted from both the diatom bio-silica and the glass are clear and visible, and the peaks can also be matched with the R6G characteristic

peaks. However, signals from the diatom basilica are three times higher than those from the glass-Ag NPs substrate, demonstrating that the diatom can contribute extra enhancement of Raman signals due to its photonics crystal effect from the ordered periodic pores structure.

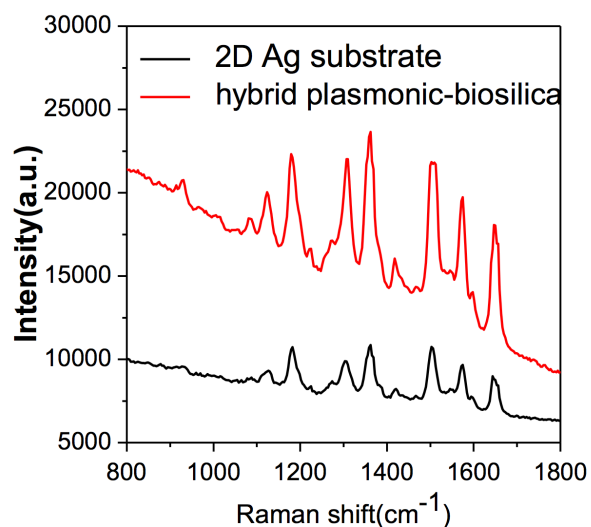


Fig. 15 Comparison of the Raman spectra conducted on diatom-Ag NPs and on glass-Ag NPs SERS substrate.

Small droplets can provide extraordinary enhancements through the evaporation-induced spontaneous flow of photonic bio-silica. Modern inkjet printers have become a novel strategy for manipulating ultra-small droplets. Recent simulations show thermocapillary forces dominate more than the viscous forces, which means the thermocapillary-induced recirculation flow can continuously transport target molecules to the surface of diatom frustules during the evaporating process, which will tremendously increase the amount and density of the probe molecules. Diatom frustules have such properties because of their micro-sub-porous structures. During the evaporating process,

the liquid will flow from the glass to the surface of the diatom frustule through the diatom capillary pores because of the hydrophilic surface of the frustules. The highly hydrophilic surface of diatom frustules is created by their abundant hydroxyl groups and porous structures.

To demonstrate that the evaporation-induced liquid flow can aid in probe molecule accumulation, and therefore, contribute extra enhancement to SERS intensity, we use inkjet printing technology to jet micro-sized analyte into diatom bio-silica. Our device is a drop-on-demand (DoD) inkjet device, which enables the inkjet printing process to be even more precise. We took the SERS measurement of different droplet groups (100 droplets, 200 droplets, 300 droplets, 400 droplets, and 500 droplets) with the same concentration of aqueous R6G solution ( $10^{-9}\text{M}$ ), and 100pl in volume for each droplet. Shown in Figure 16, as the number of droplets increases, the SERS intensity increases, meaning that ultra-small droplets can effectively transport probe molecules.

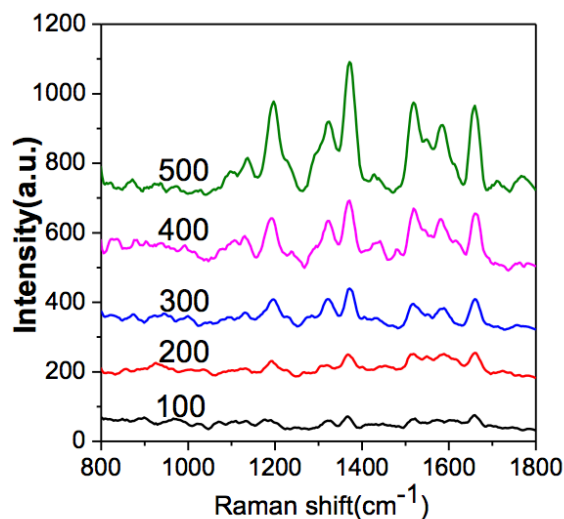


Fig. 16 Comparison of different droplets with fixed concentration of probe molecule solution.

To quantitatively see the enhancements provided by the inkjet printing strategy, we compared 400 cycles by inkjet printing method with a 100 cycle, and one droplet of 2 $\mu$ l via pipette. The concentration of the R6G is also 10<sup>-9</sup>M. There were roughly 1.2x10<sup>8</sup> R6G molecules dispensed through the pipette, but there were only roughly 2.4x10<sup>6</sup> molecules of R6G dispensed from the inkjet printer. However, Figure 17 shows a diametrically opposed result. The SERS signal from the 2 $\mu$ l droplet shows an even weaker intensity compared with the 400 droplets from the inkjet printer. This may occur for two reasons. First, the 2 $\mu$ l of liquid dispensed from the pipette was spread when the droplet attached to the substrate, covering a much larger area, thus leading to difficulties in measurement. The second reason is because of the evaporation-induced liquid flow as discussed above. Ultra-small droplets (picoliter-level) that evaporated through the caterpillar tube transported probe molecules to the surface of diatom frustules.

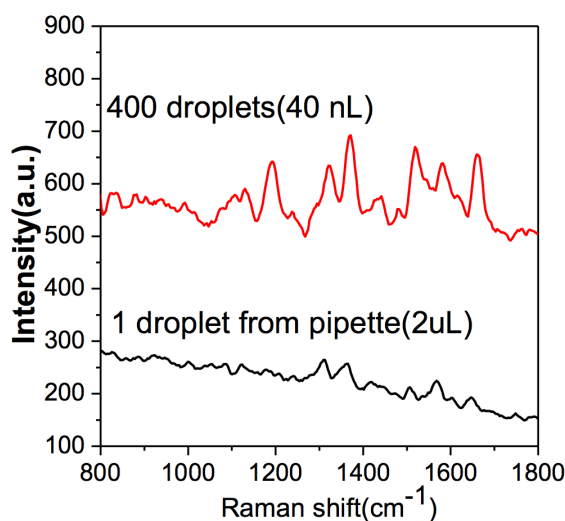


Fig. 17 Comparison of inkjet printing technology and traditional pipette delivery.

### 3.2.2.3 Droplets Affecting the Inkjet Printing Technique

For the purpose of further investigating how the number of droplets affects the molecule accumulation, we took measurements of the groups of different numbers of droplets of R6G aqueous solution at various concentrations. To fix the amount of probe molecules, we took measurements of four groups: 1 droplet at  $10^{-6}$ M R6G, 10 droplets at  $10^{-7}$ M R6G, 100 droplets at  $10^{-8}$ M R6G, and 1000 droplets at  $10^{-9}$ M R6G. The SERS spectra were collected from diatom-Ag NPs substrate and glass-Ag NPs substrate respectively. The results are shown in Figure 18(a-b).

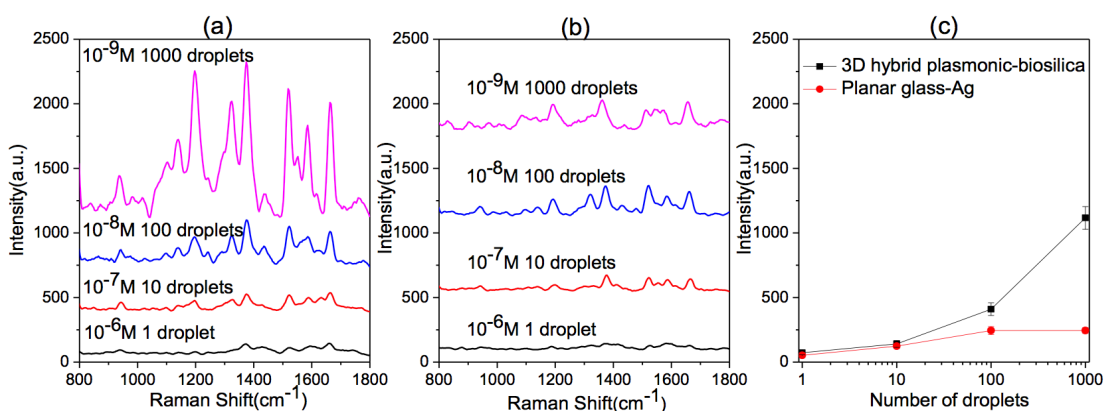


Fig. 18 Comparison of different numbers of droplets with the same amount of probe molecules on diatom-Ag NPs substrates (a), on glass-Ag NPs substrates (b) and SERS intensity collected from the most prominent peak of  $1360\text{cm}^{-1}$  versus different numbers of droplets (c).

Theoretically, the same quantities of probe molecules distributed across the same sized area should produce similar SERS intensities, but we observed that as the number of droplets increased, so did the intensity. The results are shown in Figure 18. In addition, another abnormal phenomenon was discovered from the glass-Ag NPs groups shown in Figure (b); the 1-droplet and 10-droplet groups showed very unobvious signals, but as the number of droplets increased, we observed obvious peaks that matched the characteristic

peaks of R6G. This phenomenon shows that the diffusion force is much weaker than the convection force. This means that molecules are more likely to be transported through a continuous process, but not a single-second evaporating process.

Strangely enough, we also seemed to receive a similar signal from both 10-droplet groups on diatom-Ag NPs substrate and glass-Ag NPs substrate respectively. To investigate further, we plotted the SERS signal collected from the most prominent peak at  $1360\text{cm}^{-1}$  versus different droplet groups as shown in Figure 18(c). The increasing rate difference enlarged with the increasing number of droplets. The phenomenon of the similar signal from the 10 droplets group may have resulted from the coffee ring, as soon as the number of droplets reached the 100-droplet level, the coffee ring effect was saturated, and at this saturation point, the convection force was balanced with the diffusion force. After the saturating point, the convection begins to dominate.

#### *3.2.2.4 Single molecule detection achievement*

After observing that molecules were more likely to be transported through a continuous process, and that the more droplets that were printed, the faster the intensity increased, we decided to lower the detection level. An amount of 2000 droplets of  $10^{-16}\text{M}$  R6G aqueous solution was dispensed by the inkjet printer on a diatom-Ag NPs substrate. Only around 16 R6G molecules were distributed across the substrate. In theory, it is very difficult to detect such ultra-low density R6G molecules; there was, at most, one molecule that appeared under the laser spot. However, we managed to pick up the signal

shown in Figure 19. There was roughly a 30% chance for the probe molecules to appear on the diatom, thus proving that the diatom frustules can accumulate molecules.

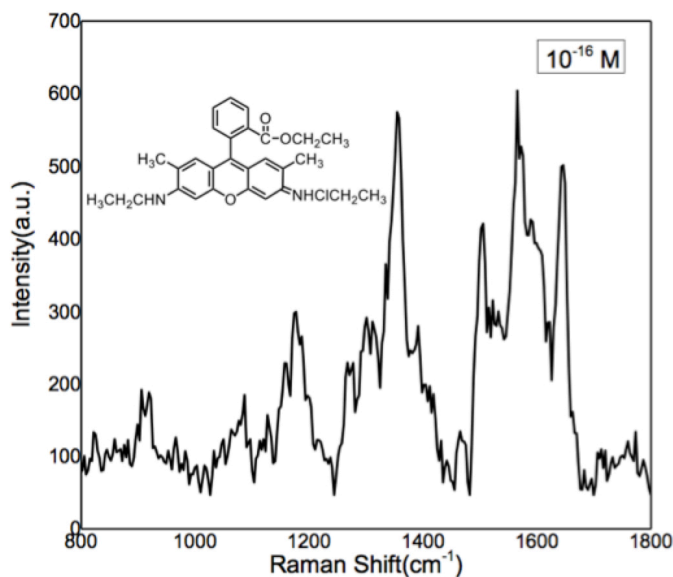


Fig. 19 Ultra-sensitive single molecule detection with diatom substrate by an inkjet printer dispensing 2000 droplets: SERS spectra of  $10^{-16}$  M R6G aqueous solution

### 3.2.3 Technic Demonstration by Inkjet Printing on TNT Sensing

To confirm the result of the single R6G molecule detection, a very similar measurement was conducted using trinitrotoluene (TNT) as the probe molecule. TNT is one of the most common explosives currently available. Although researchers have dramatically reduced the lower limit of TNT detection using the SERS method, because of the low affinity between TNT and nanoparticles, surface functionalization of the SERS substrates is generally required, making the development an ultra-sensitive, label-free method of TNT detection very difficult; no such label-free SERS method has shown

decent sensitivity thus far. As shown in Figure 20, a distinct TNT signal was detected at  $10^{-12}$  M, whereas the signal could only be detected at  $10^{-8}$  M using the conventional pipette. In addition, the total volume of solution consumed was only 200 nL. The results correspond to  $4.5 \times 10^{-17}$  grams of TNT, or 1193 TNT molecules, indicating a sensitivity enhancement of  $10^7$  times. The mapping image (Figure 21) corroborates the assertion that an EF at  $10^{-7}$  M was reached via the inkjet printing technique. Both results have demonstrated that the evaporation-induced fluid flow makes enormous contributions to molecule accumulation.

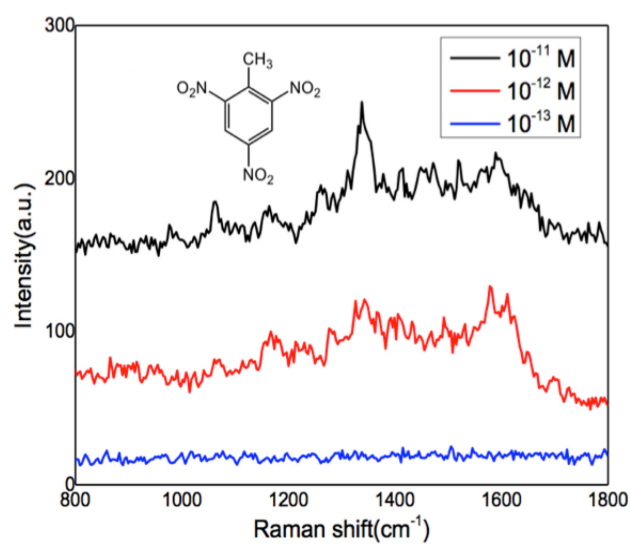


Fig. 20 Ultra-sensitive single molecule detection with diatom substrate by an inkjet printer dispensing 2000 droplets SERS spectra of TNT with concentration at  $10^{-11}$  M,  $10^{-12}$  M, and  $10^{-13}$  M.

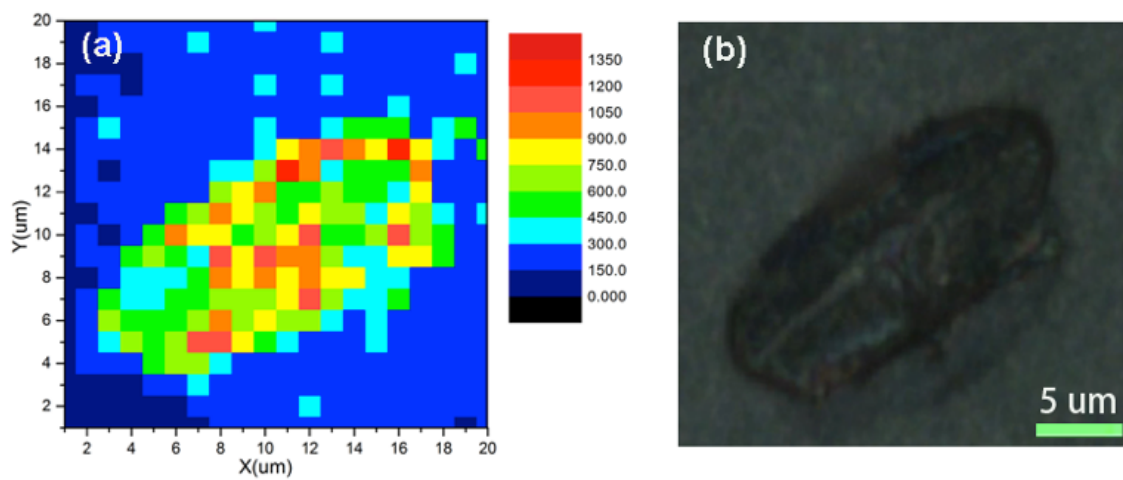


Fig. 21 SERS mapping image collected from  $10^{-5}$ M TNT aqueous solution with 400 droplets dispersed on a single diatom and corresponding diatom image (b).

## Chapter 4: Conclusion

### Conclusion

In conclusion, we have observed the effect of inkjet printing technology on porous-structured photonic crystal bio-silica-based SERS sensing. The inkjet printing method enabled the delivery of ultra-small droplets of analyte solution with pinpoint precision, allowing for ultra-low analyte consumption and accurate targeting. In addition, we discover an evaporation-induced spontaneous flow effect from the evaporating process of small droplets. In comparison with the traditional pipette-based SERS sensing, the evaporation-induced spontaneous flow effect achieved by the inkjet printing method resulted in a significant enhancement of SERS intensity using micro-sized inkjet-printed liquid droplets. Unlike other opto-fluidic sensing options, we observed that the evaporation process of the ultra-small liquid droplets provided a strong convection flow which resulted in substantial molecule accumulation on the surface of diatom, greatly increasing the density of the target molecules, and making it possible to enable a single-molecule-level of detection, as was verified by our experiments. The effect of molecule accumulation can be improved by multiple cycles delivered by inkjet printer. Inkjet printing technology enhanced efficacy by  $10^6$ - $10^7$  times, aiding in the single-molecule-level detection of R6G and  $10^{-12}$ M-level, label-free TNT detection in aqueous solution.

## Chapter 5: Clarification and Acknowledgement

1. Fig. 7 was drawn by Prof. Tan(Washington State University - Vancouver)<sup>72</sup>
2. SEM images in Fig. 8, Fig. 10 and Fig. 11 were captured by Xinyuan Chong
3. Fig. 9(c) and (d) were plotted by Xianming Kong
4. Fluorescence images in Fig. 13 and Fig. 14 were joint work with Xianming Kong
5. Fluorescence spectra in Fig. 14(b) and (c) were joint work with Xianming Kong
6. Fig. 18(c) were joint work with Xianming Kong, and plotted by Xianming Kong
7. TNT sensing in Fig. 20 and Fig. 21 were joint work with Xianming Kong
8. Parameters in Table 1 were provided by Hewlett-Packard(HP Inc., Corvallis, OR)
9. The in-situ synthesized substrate used throughout the experience were prepared by Xianming Kong
10. The Ag NPs colloid used throughout the experience were joint work with Xianming Kong
11. The diatom substrates used throughout the experience were prepared by Paul LeDuff from Dr. Rorrer's research group

## Chapter 6: Reference

## Reference

1. Graves, P. R., & Gardiner, D. J. (1989). Practical Raman Spectroscopy.
2. Fleischmann, M., Hendra, P. J., Hill, I. R., & Pemble, M. E. (1981). Enhanced Raman spectra from species formed by the coadsorption of halide ions and water molecules on silver electrodes. *Journal of Electroanalytical Chemistry and Interfacial Electrochemistry*, 117(2), 243-255.
3. Jeanmaire, D. L., & Van Duyne, R. P. (1977). Surface Raman spectroelectrochemistry: Part I. Heterocyclic, aromatic, and aliphatic amines adsorbed on the anodized silver electrode. *Journal of Electroanalytical Chemistry and Interfacial Electrochemistry*, 84(1), 1-20.
4. Pettinger, B. (1986). Light scattering by adsorbates at Ag particles: Quantum-mechanical approach for energy transfer induced interfacial optical processes involving surface plasmons, multipoles, and electron-hole pairs. *The Journal of chemical physics*, 85(12), 7442-7451.
5. Willets, K. A. (2014). Super-resolution imaging of SERS hot spots. *Chemical Society Reviews*, 43(11), 3854-3864.
6. Xu, X., Kim, K., Li, H., & Fan, D. L. (2012). Ordered arrays of Raman nanosensors for ultrasensitive and location predictable biochemical detection. *Advanced Materials*, 24(40), 5457-5463.
7. Zhao, X., Xue, J., Mu, Z., Huang, Y., Lu, M., & Gu, Z. (2015). Gold nanoparticle incorporated inverse opal photonic crystal capillaries for optofluidic surface enhanced Raman spectroscopy. *Biosensors and Bioelectronics*, 72, 268-274.
8. Guo, Y., Khaing Oo, M. K., Reddy, K., & Fan, X. (2011). Ultrasensitive optofluidic surface-enhanced Raman scattering detection with flow-through multihole capillaries. *Acs Nano*, 6(1), 381-388.
9. Driskell, J. D., Lipert, R. J., & Porter, M. D. (2006). Labeled gold nanoparticles immobilized at smooth metallic substrates: systematic investigation of surface

- plasmon resonance and surface-enhanced Raman scattering. *The Journal of Physical Chemistry B*, 110(35), 17444-17451.
10. Mok, J., Mindrinos, M. N., Davis, R. W., & Javanmard, M. (2014). Digital microfluidic assay for protein detection. *Proceedings of the National Academy of Sciences*, 111(6), 2110-2115.
  11. Cui, F., Rhee, M., Singh, A., & Tripathi, A. (2015). Microfluidic sample preparation for medical diagnostics. *Annual review of biomedical engineering*, 17, 267-286.
  12. Bruchmann, J., Sachsenheimer, K., Rapp, B. E., & Schwartz, T. (2015). Multi-channel microfluidic biosensor platform applied for online monitoring and screening of biofilm formation and activity. *PloS one*, 10(2), e0117300.
  13. Fan, X., & White, I. M. (2011). Optofluidic microsystems for chemical and biological analysis. *Nature photonics*, 5(10), 591-597.
  14. Martinez, A. W., Phillips, S. T., Whitesides, G. M., & Carrilho, E. (2009). Diagnostics for the developing world: microfluidic paper-based analytical devices.
  15. Osborn, J. L., Lutz, B., Fu, E., Kauffman, P., Stevens, D. Y., & Yager, P. (2010). Microfluidics without pumps: reinventing the T-sensor and H-filter in paper networks. *Lab on a Chip*, 10(20), 2659-2665.
  16. Dimov, I. K., Basabe-Desmonts, L., Garcia-Cordero, J. L., Ross, B. M., Ricco, A. J., & Lee, L. P. (2011). Stand-alone self-powered integrated microfluidic blood analysis system (SIMBAS). *Lab on a Chip*, 11(5), 845-850.
  17. Monat, C., Domachuk, P., & Eggleton, B. J. (2007). Integrated optofluidics: A new river of light. *Nature photonics*, 1(2), 106-114.
  18. Psaltis, D., Quake, S. R., & Yang, C. (2006). Developing optofluidic technology through the fusion of microfluidics and optics. *Nature*, 442(7101), 381-386.
  19. Pang, L., Chen, H. M., Freeman, L. M., & Fainman, Y. (2012). Optofluidic devices and applications in photonics, sensing and imaging. *Lab on a Chip*, 12(19), 3543-3551.
  20. Hoa, X. D., Kirk, A. G., & Tabrizian, M. (2007). Towards integrated and sensitive surface plasmon resonance biosensors: a review of recent progress. *Biosensors and Bioelectronics*, 23(2), 151-160.

21. Anker, J. N., Hall, W. P., Lyandres, O., Shah, N. C., Zhao, J., & Van Duyne, R. P. (2008). Biosensing with plasmonic nanosensors. *Nature materials*, 7(6), 442-453.
22. Stewart, M. E., Anderton, C. R., Thompson, L. B., Maria, J., Gray, S. K., Rogers, J. A., & Nuzzo, R. G. (2008). Nanostructured plasmonic sensors. *Chemical reviews*, 108(2), 494-521.
23. Brolo, A. G. (2012). Plasmonics for future biosensors. *Nature Photonics*, 6(11), 709-713.
24. Choi, I., & Choi, Y. (2012). Plasmonic nanosensors: Review and prospect. *IEEE Journal of Selected Topics in Quantum Electronics*, 18(3), 1110-1121.
25. Raschke, G., Kowarik, S., Franzl, T., Sönnichsen, C., Klar, T. A., Feldmann, J., ... & Kürzinger, K. (2003). Biomolecular recognition based on single gold nanoparticle light scattering. *Nano lett*, 3(7), 935-938.
26. Sun, Y., & Fan, X. (2011). Optical ring resonators for biochemical and chemical sensing. *Analytical and bioanalytical chemistry*, 399(1), 205-211.
27. De Vos, K., Bartolozzi, I., Schacht, E., Bienstman, P., & Baets, R. (2007). Silicon-Insulator microring resonator for sensitive and label-free biosensing. *Optics express*, 15(12), 7610-7615.
28. Chao, C. Y., Fung, W., & Guo, L. J. (2006). Polymer microring resonators for biochemical sensing applications. *IEEE Journal of selected Topics in quantum electronics*, 12(1), 134-142.
29. Vollmer, F., & Arnold, S. (2008). Whispering-gallery-mode biosensing: label-free detection down to single molecules. *Nature methods*, 5(7), 591-596.
30. Jensen, J. B., Pedersen, L. H., Hoiby, P. E., Nielsen, L. B., Hansen, T. P., Folkenberg, J. R., ... & Bjarklev, A. (2004). Photonic crystal fiber based evanescent-wave sensor for detection of biomolecules in aqueous solutions. *Optics letters*, 29(17), 1974-1976.
31. Chow, E., Grot, A., Mirkarimi, L. W., Sigalas, M., & Girolami, G. (2004). Ultracompact biochemical sensor built with two-dimensional photonic crystal microcavity. *Optics letters*, 29(10), 1093-1095.

32. Kabashin, A. V., Evans, P., Pastkovsky, S., Hendren, W., Wurtz, G. A., Atkinson, R., ... & Zayats, A. V. (2009). Plasmonic nanorod metamaterials for biosensing. *Nature materials*, 8(11), 867-871.
33. Sheehan, P. E., & Whitman, L. J. (2005). Detection limits for nanoscale biosensors. *Nano letters*, 5(4), 803-807.
34. Eftekhari, F., Escobedo, C., Ferreira, J., Duan, X., Girotto, E. M., Brolo, A. G., ... & Sinton, D. (2009). Nanoholes as nanochannels: flow-through plasmonic sensing. *Analytical chemistry*, 81(11), 4308-4311.
35. Guo, Y., Li, H., Reddy, K., Shelar, H. S., Nittoor, V. R., & Fan, X. (2011). Optofluidic Fabry–Pérot cavity biosensor with integrated flow-through micro-/nanochannels. *Applied Physics Letters*, 98(4), 041104.
36. Huang, M., Yanik, A. A., Chang, T. Y., & Altug, H. (2009). Sub-wavelength nanofluidics in photonic crystal sensors. *Optics express*, 17(26), 24224-24233.
37. Yablonovitch, E. (1987). Inhibited spontaneous emission in solid-state physics and electronics. *Physical review letters*, 58(20), 2059.
38. John, S. (1987). Strong localization of photons in certain disordered dielectric superlattices. *Physical review letters*, 58(23), 2486.
39. Notomi, M., Yamada, K., Shinya, A., Takahashi, J., Takahashi, C., & Yokohama, I. (2001). Extremely large group-velocity dispersion of line-defect waveguides in photonic crystal slabs. *Physical Review Letters*, 87(25), 253902.
40. Fan, S., & Joannopoulos, J. D. (2002). Analysis of guided resonances in photonic crystal slabs. *Physical Review B*, 65(23), 235112.
41. Chen, X., Wang, A. X., Chakravarty, S., & Chen, R. T. (2009). Electrooptically-active slow-light-enhanced silicon slot photonic crystal waveguides. *IEEE Journal of Selected Topics in Quantum Electronics*, 15(5), 1506-1509.
42. Lin, C. Y., Wang, X., Chakravarty, S., Lee, B. S., Lai, W., Luo, J., ... & Chen, R. T. (2010). Electro-optic polymer infiltrated silicon photonic crystal slot waveguide modulator with 23 dB slow light enhancement. *Applied Physics Letters*, 97(9), 194.

43. Wang, X., Chakravarty, S., Lee, B. S., Lin, C., & Chen, R. T. (2009). Ultraefficient control of light transmission through photonic potential barrier modulation. *Optics letters*, 34(20), 3202-3204.
44. Wang, X., Lin, C. Y., Chakravarty, S., Luo, J., Jen, A. K. Y., & Chen, R. T. (2011). Effective in-device  $r_{33}$  of 735 pm/V on electro-optic polymer infiltrated silicon photonic crystal slot waveguides. *Optics letters*, 36(6), 882-884.
45. Lai, W. C., Chakravarty, S., Wang, X., Lin, C., & Chen, R. T. (2011). Photonic crystal slot waveguide absorption spectrometer for on-chip near-infrared spectroscopy of xylene in water. *Applied Physics Letters*, 98(2), 7.
46. Lai, W. C., Chakravarty, S., Wang, X., Lin, C., & Chen, R. T. (2011). On-chip methane sensing by near-IR absorption signatures in a photonic crystal slot waveguide. *Optics letters*, 36(6), 984-986.
47. Xu, X., Hasan, D., Wang, L., Chakravarty, S., Chen, R. T., Fan, D. L., & Wang, A. X. (2012). Guided-mode-resonance-coupled plasmonic-active SiO<sub>2</sub> nanotubes for surface enhanced Raman spectroscopy. *Applied physics letters*, 100(19), 191114.
48. Round, F. E., Crawford, R. M., & Mann, D. G. (1990). *Diatoms: biology and morphology of the genera*. Cambridge University Press.
49. Joannopoulos, J. D., Johnson, S. G., Winn, J. N., & Meade, R. D. (2011). *Photonic crystals: molding the flow of light*. Princeton university press.
50. De Stefano, L., Maddalena, P., Moretti, L., Rea, I., Rendina, I., De Tommasi, E., ... & De Stefano, M. (2009). Nano-biosilica from marine diatoms: a brand new material for photonic applications. *Superlattices and Microstructures*, 46(1), 84-89.
51. Quintero-Torres, R., Aragón, J. L., Torres, M., Estrada, M., & Cros, L. (2006). Strong far-field coherent scattering of ultraviolet radiation by holococcolithophores. *Physical Review E*, 74(3), 032901.
52. Whitty, J. (2011, January 20). PSYCHEDELIC DIATOMS. Retrieved from <http://deepbluehome.blogspot.com/2011/01/psychedelic-diatoms.html>
53. Jeffryes, C., Campbell, J., Li, H., Jiao, J., & Rorrer, G. (2011). The potential of diatom nanobiotechnology for applications in solar cells, batteries, and electroluminescent devices. *Energy & Environmental Science*, 4(10), 3930-3941.

54. Song, M. K., Park, S., Alamgir, F. M., Cho, J., & Liu, M. (2011). Nanostructured electrodes for lithium-ion and lithium-air batteries: the latest developments, challenges, and perspectives. *Materials Science and Engineering: R: Reports*, 72(11), 203-252.
55. Zhang, Y., Liu, G., & Li, H. (2006). Development of a micro swimming robot using optimised giant magnetostrictive thin films. *Applied Bionics and Biomechanics*, 3(3), 161-170.
56. Jeffryes, C., Solanki, R., Rangineni, Y., Wang, W., Chang, C. H., & Rorrer, G. L. (2008). Electroluminescence and photoluminescence from nanostructured diatom frustules containing metabolically inserted germanium. *Advanced Materials*, 20(13), 2633-2637.
57. Qin, T., Gutu, T., Jiao, J., Chang, C. H., & Rorrer, G. L. (2008). Photoluminescence of silica nanostructures from bioreactor culture of marine diatom *Nitzschia frustulum*. *Journal of nanoscience and nanotechnology*, 8(5), 2392-2398.
58. Losic, D., Mitchell, J. G., Lal, R., & Voelcker, N. H. (2007). Rapid Fabrication of Micro-and Nanoscale Patterns by Replica Molding from Diatom Biosilica. *Advanced Functional Materials*, 17(14), 2439-2446.
59. Losic, D., Rosengarten, G., Mitchell, J. G., & Voelcker, N. H. (2006). Pore architecture of diatom frustules: potential nanostructured membranes for molecular and particle separations. *Journal of nanoscience and nanotechnology*, 6(4), 982-989.
60. Gale, D. K., Gutu, T., Jiao, J., Chang, C. H., & Rorrer, G. L. (2009). Photoluminescence detection of biomolecules by antibody-functionalized diatom biosilica. *Advanced Functional Materials*, 19(6), 926-933.
61. Miller, O. J., El Harrak, A., Mangeat, T., Baret, J. C., Frenz, L., El Debs, B., ... & Galvan, M. (2012). High-resolution dose-response screening using droplet-based microfluidics. *Proceedings of the National Academy of Sciences*, 109(2), 378-383.
62. Baluya, D. L., Garrett, T. J., & Yost, R. A. (2007). Automated MALDI matrix deposition method with inkjet printing for imaging mass spectrometry. *Analytical chemistry*, 79(17), 6862-6867.

63. Derby, B. (2008). Bioprinting: inkjet printing proteins and hybrid cell-containing materials and structures. *Journal of Materials Chemistry*, 18(47), 5717-5721.
64. Hoppmann, E. P., Wei, W. Y., & White, I. M. (2014). Inkjet-printed fluidic paper devices for chemical and biological analytics using surface enhanced Raman spectroscopy. *IEEE Journal of Selected Topics in Quantum Electronics*, 20(3), 195-204.
65. Yu, W. W., & White, I. M. (2010). Inkjet printed surface enhanced Raman spectroscopy array on cellulose paper. *Analytical chemistry*, 82(23), 9626-9630.
66. Wei, W. Y., & White, I. M. (2013). Chromatographic separation and detection of target analytes from complex samples using inkjet printed SERS substrates. *Analyst*, 138(13), 3679-3686.
67. Lee, H. H., Chou, K. S., & Huang, K. C. (2005). Inkjet printing of nanosized silver colloids. *Nanotechnology*, 16(10), 2436.
68. Restaino, S. M., & White, I. M. (2015, March). Inkjet-fabricated surface enhanced Raman spectroscopy (SERS) sensors on paper for biosensing. In SPIE BiOS (pp. 93140R-93140R). International Society for Optics and Photonics.
69. Lee, P. C., & Meisel, D. (1982). Adsorption and surface-enhanced Raman of dyes on silver and gold sols. *J. Phys. Chem*, 86(17), 3391-3395.
70. Yang, J., Zhen, L., Ren, F., Campbell, J., Rorrer, G. L., & Wang, A. X. (2015). Ultra-sensitive immunoassay biosensors using hybrid plasmonic-biosilica nanostructured materials. *Journal of biophotonics*, 8(8), 659-667.
71. Kong, X., Xi, Y., Le Duff, P., Chong, X., Li, E., Ren, F., ... & Wang, A. X. (2017). Detecting explosive molecules from nanoliter solution: A new paradigm of SERS sensing on hydrophilic photonic crystal biosilica. *Biosensors and Bioelectronics*, 88, 63-70.
72. Kong, X., Xi, Y., LeDuff, P., Li, E., Liu, Y., Cheng, L. J., ... & Wang, A. X. (2016). Optofluidic sensing from inkjet-printed droplets: the enormous enhancement by evaporation-induced spontaneous flow on photonic crystal biosilica. *Nanoscale*, 8(39), 17285-17294.